Dynamics of an ultracold weakly bound heteronuclear diatomic molecule in an ultrashort laser pulse

Zi-Ang Li (李子昂), Xu-Hui Bai (白旭辉), Yi-De Yin (尹益德), Gao-Ren Wang (王高仁),* and Shu-Lin Cong (丛书林)
School of Physics, Dalian University of Technology, Dalian 116024, China

(Received 19 August 2023; revised 7 February 2024; accepted 27 February 2024; published 18 March 2024)

We propose a theoretical model used for dynamically manipulating an ultracold weakly bound heteronuclear alkali-metal diatomic molecule by a nonresonant single-cycle THz laser pulse. Taking the ^{6}Li ^{23}Na molecule as an example, we first calculate the variation of the weakly bound state and quasibound state as a function of external electric field, and then reveal abundant interference patterns during and after the laser pulse due to the superpositions between states involving weakly bound state, scattering state, and quasibound state. Moreover, one can map out the nodes of the probability density of the weakly bound molecules by measuring the wavepacket dynamics.

DOI: 10.1103/PhysRevA.109.033311

I. INTRODUCTION

The molecules just below the scattering threshold possess unique properties [1]. These weakly bound molecules are bridges between atoms and the deeply bound molecules [2]. Due to the tiny binding energy, the weakly bound molecules are fragile at room temperature. As a result, ultracold quantum gas is an ideal platform to study weakly bound molecules. One can produce weakly bound molecules out of ultracold quantum gas via two-photon photoassociation [3], microwave photoassociation [4,5], magnetoassociation [6,7], or electroassociation [8]. Currently, ultracold weakly bound molecules consisting of two atoms [3–7], an atom and a ground-state diatomic molecules [9], or two diatomic molecules [10] have been produced, respectively. The availability of these weakly bound molecules enabled many intriguing applications. A molecular version of intensity interferometry has been realized with weakly bound molecules and the density-density correlations were measured [11]. The weakly bound molecules were prepared in the second Bloch band of an optical lattice which can simulate exotic orbital physics [12]. In addition, the weakly bound molecules were used to study controlled state-to-state reaction dynamics [13,14], investigate the ionization dynamics [15], achieve molecular clock [16,17], search for new gravitylike forces [18], and so on.

The control of the weakly bound molecules via external fields has attracted much attention. The properties of the weakly bound molecule in a static electric field [19,20], static magnetic field [6], or continuous-wave nonresonant laser field [21] have been analyzed. Recently, the dynamics of weakly bound ^{4}He$_2$ molecules induced by an ultrafast laser pulse were studied theoretically [22] and experimentally [23]. Alignment signals have been observed and the wavepacket dynamics of the weakly bound state in the ultrafast laser field is significantly different from widely studied wavepacket dynamics of the rigid-rotor-like molecules [22,23]. Inspired by these works, we study the dynamics of the weakly bound heteronuclear diatomic molecules composed of alkali-metal atoms in the ultrafast laser field. Various kinds of weakly bound heteronuclear alkali-metal diatomic molecules have been prepared experimentally [7,24–31]. The heteronuclear molecule has permanent dipole moment, while the homonuclear molecule ^{4}He$_2$ did not. As a result, orientation signals, in addtion to the alignment signals, were observed for heteronuclear molecules. Moreover, the heteronuclear alkali-metal diatomic molecule has more than one bound state. In contrast, the ^{4}He$_2$ molecule has only one bound state. The influence of these bound states on the wavepacket dynamics are explored in this work. In addition, the influence of the laser parameters, such as electric field amplitude and duration time on the dynamics are studied.

This paper is organized as follows. In Sec. II, the theoretical methods are described. In Sec. III, the results and discussions are given. A conclusion is drawn in Sec. IV.

II. THEORETICAL METHODS

In this work, we take the weakly bound ^{6}Li ^{23}Na molecules as an illustration, which have been produced in the vicinity of Feshbach resonances [30]. To fully describe the weakly bound ^{6}Li ^{23}Na molecules, an intrinsic multichannel interaction needs to be considered [32]. Nevertheless, the single-channel approximation is often applied [33]. The weakly bound ^{6}Li ^{23}Na molecule has mainly a triplet character [34]. In the following, the ^{6}Li ^{23}Na molecule in $a^3\Sigma^+$ state is chosen as a prototype. A nonresonant laser pulse is applied to induce the wavepacket dynamics. Within the Born-Oppenheimer approximation, the interaction of the ^{6}Li ^{23}Na molecule and a nonresonant laser pulse can be described by

*gaoren.wang@dlut.edu.cn

the Hamiltonian [20,35,36]

$$\hat{H} = -\frac{1}{2\mu R}\frac{\partial^2}{\partial R^2}R + \hat{V}(R) + \frac{\hat{l}^2}{2\mu R^2} + \hat{V}_\varepsilon(R,t), \qquad (1)$$

where μ is the reduced mass and R is the internuclear distance. $\hat{V}(R)$ denotes the interatomic potential-energy operator. $\hat{l}$ denotes the partial-wave operator and the third term of the Hamiltonian describes the rotation energy of the system. The average effect of the interaction $\hat{V}_\varepsilon(R,t)$ between the permanent dipole moment of the heteronuclear diatomic molecule $D(R)$ and the time-dependent electric field of a nonresonant laser pulse $\varepsilon(t)$ is negligible if the duration of the laser pulse is much larger than the circle of the laser pulse [37,38]. In this work, a nonresonant single-cycle THz pulse is adopted and the laser duration is comparable to its cycle. Hence, the effect of $\hat{V}_\varepsilon$ cannot be ignored. The expression of $\hat{V}_\varepsilon$ is given by

$$\hat{V}_\varepsilon(R,t) = -\varepsilon(t)D(R)\cos\theta, \qquad (2)$$

where the direction of the electric field is set to be the space-fixed z axis and θ is the angle between the interatomic axis and the z axis.

The electric field strength of the nonresonant THz laser pulse is defined by [39,40]

$$\varepsilon(t) = \varepsilon[1 - 2\kappa(t-t_0)^2]e^{-\kappa(t-t_0)^2}, \qquad (3)$$

where ε is the electric field amplitude. κ is related to the pulse duration δ by $\kappa = 6/\delta^2$ [40]. The parameter δ is the time difference between the two values of t at which $\varepsilon(t)$ is minimum. t_0 is the central time. In the following, the quasibound and bound states in the static electric field are calculated and $\varepsilon(t)$ is set to be a constant ε in this case. The effect of the polarizability, which was commonly involved in the studies of homonuclear molecules [22,23,41,42], is expected to be much smaller than that of the dipole moment and is omitted [19,20,35,36,43,44].

In the realistic system, the energy of the weakly bound molecule can be tuned by an external magnetic field in the vicinity of a Feshbach resonance. To mimic the tuning of the weakly bound molecule, the interatomic potential $V(R)$ is set to be $V(R) = V_{a^3\Sigma^+}(R) + V_\alpha(R)$, where $V_{a^3\Sigma^+}(R)$ is the potential curve of the $a^3\Sigma^+$ state

$$V_\alpha(R) = \begin{cases} \alpha(R-R_e)^2 & R < R_e, \\ 0 & R \geqslant R_e, \end{cases} \qquad (4)$$

where $R_e = 4.63$ Å is the equilibrium internuclear distance of the $a^3\Sigma^+$ state [45] and α is the modification factor. The last s-wave bound state supported by potential $V(R)$ is the weakly bound state we are interested in. By varying the value of α, the energy of the weakly bound state changes. The potential energy curve $V_{a^3\Sigma^+}(R)$ [45] and the permanent dipole moment $D(R)$ [46] are shown in Fig. 1. In Ref. [22], it was found that the quasibound state can turn into a field-induced bound state, and has a significant influence on the wavepacket dynamics. In the following, α is set to be -1.58307×10^8 GHz/Å^2 and the potential $V(R)$ supports an s-wave least bound state at 340 MHz, and a p-wave quasibound state at 0.5 MHz.

To calculate the bound and quasibound states in static electric field, we set $\varepsilon(t)$ to be a constant. The corresponding stationary Schrödinger equation with Hamiltonian Eq. (1) is solved by the mapped Fourier grid Hamiltonian method (MFGH) [47,48] to obtain the bound-state energies. To determine the positions of the quasibound states, the elastic cross section is calculated by the log-derivative method [49].

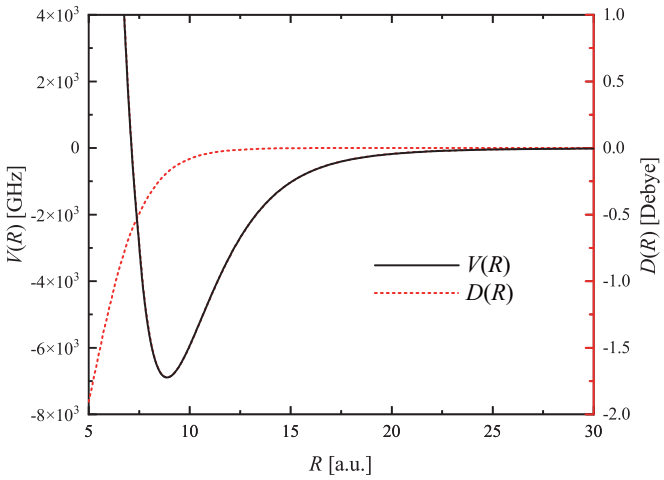

FIG. 1. The potential energy curve $V(R)$ (black solid line) [45] and the permanent dipole moment $D(R)$ (red dotted line) [46] as a function of the internuclear distance R of the ^{6}Li ^{23}Na molecule in $a^3\Sigma^+$ state.

To calculate the wavepacket dynamics of the system in laser field, the time-dependent Schrödinger equation with Hamiltonian Eq. (1) is solved. The molecule is supposed to be prepared in the s-wave least bound state initially. The evolution operator is expanded in Chebyshev polynomials [50,51].

In previous studies of the homonuclear molecule ^{4}He$_2$ [22,23], the laser field induces wavepacket dynamics via the interaction with the polarizability. Thus, the l-wave state can be coupled with the l'-wave state, where l' equals l-2, l, or $l+2$. So alignment $C_2(R,t)$ is calculated to visualize the dynamics, which is defined as [22]

$$C_2(R,t) = \frac{\int_0^\pi \Psi^*(R,\theta,t)\cos^2\theta\Psi(R,\theta,t)\sin\theta d\theta}{\int_0^\pi |\Psi(R,\theta,t)|^2\sin\theta d\theta}, \qquad (5)$$

where $\Psi(R,\theta,t)$ denotes the time-dependent wave function. In this work, we investigate the heteronuclear ^{6}Li^{23}Na molecule. The laser field interacts mainly with the permanent dipole moment. Thus, the l-wave state can be coupled with the l'-wave state, where l' equals l-1, or $l+1$. In addition $C_2(R,t)$, we can also use orientation $C_1(R,t)$ to visualize dynamics, which is defined as

$$C_1(R,t) = \frac{\int_0^\pi \Psi^*(R,\theta,t)\cos\theta\Psi(R,\theta,t)\sin\theta d\theta}{\int_0^\pi |\Psi(R,\theta,t)|^2\sin\theta d\theta}. \qquad (6)$$

$C_2(R,t)$ and $C_1(R,t)$ are functions of the internuclear distance R and time t and reflect the population distribution of the wavepacket in different partial-wave states. It has been shown that $C_2(R,t)$ can be measured experimentally by the Coulomb explosion imaging [23]. The angular distribution of the initial s-wave weakly bound state is isotropic, the corresponding $C_2(R,t)$ is equal to 1/3, and $C_1(R,t)$ is equal to 0. When the laser pulse is turned on, part of the population will be transferred to the high-partial-wave states. Accordingly, $C_2(R,t)$

and $C_1(R,t)$ will deviate from $1/3$ and 0, respectively, which indicates the response of the weakly bound ^{6}Li ^{23}Na molecule to the nonresonant laser pulse.

In the calculation, the lowest ten partial-wave states are included to obtain convergent results. In an electric field, different partial-wave states are coupled, and the rational quantum number l is not a good quantum number. Nevertheless, each eigenstate at $\varepsilon \neq 0$ can be associated with a state described by quantum number l at $\varepsilon = 0$. Hence, we use $\tilde{l}$ to label the states at $\varepsilon \neq 0$ in the following. The magnetic quantum number m is conserved. Moreover, the $\pm m$ states are degenerated in an electric field. In the following, we will label the state by the absolute value of m.

III. RESULTS AND DISCUSSIONS

A. Variation of quasibound state with electric field

In this subsection, we calculate the variation of a p-wave quasibound state with a static electric field and show when the quasibound state turns into a field-induced bound state.

Figure 2(a) shows the p-wave elastic cross sections $\sigma_p^{|m|=1}$ versus the collision energy $E_{\rm col}$ at different electric field strengths. In the calculation, $|m|$ equals 1. As shown by the black solid line in Fig. 2(a) the cross section calculated at $\varepsilon = 0$ has a peak at $E_{\rm col} = 0.5$ MHz which implies the existence of a p-wave quasibound state. As the strength of the external electric field becomes larger, the peak of the cross section $\sigma_p^{|m|=1}$ shifts to smaller collision energy. The variation of the peak position of cross sections $\sigma_p^{|m|=1}$ as a function of the electric field is shown in Fig. 2(b) by the black dots. It is indicated that the energy of the p-wave quasibound state with $|m| = 1$ decreases with the increase of the electric field strength. If the electric-field strength is increased to $\varepsilon = 5.8 \times 10^{-5}$ a.u., the p-wave quasibound state crosses the threshold, and a field-induced zero-energy resonance occurs. If the electric-field strength is larger than $\varepsilon = 5.8 \times 10^{-5}$ a.u., the p-wave quasibound state turns into a field-induced bound state. The p-wave field-induced bound states are shown by black solid line in Fig. 2(b).

Figure 3(a) shows the p-wave elastic cross sections $\sigma_p^{m=0}$ versus the collision energy $E_{\rm col}$ at different electric-field strengths. In the calculation, m equals 0. In the absence of the external electric field, the peak of the p-wave cross section $\sigma_p^{m=0}$ occurs at $E_{\rm col} = 0.5$ MHz as shown by the black solid line in Fig. 3(a), which indicates the presence of a p-wave quasibound state with $m = 0$. The peak positions of cross sections $\sigma_p^{m=0}$ as a function of the electric field in the range $\varepsilon = 0 - 1.5 \times 10^{-4}$ a.u. are shown by black dots in Fig. 3(b). Different from the case with $|m| = 1$, the peak positions with $m = 0$ increase with the increase of the electric-field strength in such a strength range. However, when the electric-field strength is increased to 2.0×10^{-4} a.u., the cross section has no distinct peak, as shown by the purple double-dot-dashed line in Fig. 3(a). Thus it is difficult to locate the position of the p-wave $m = 0$ quasibound state precisely. This is the result of the strong coupling between the p-wave channel and the s-wave channel in such a strong electric field. The s-wave channel has no rotational barrier and does not support quasibound states. Nevertheless, the energy of the p-wave electric-field-induced bound state can be calculated by the MFGH method and is shown by the black solid line in Fig. 3(b). The zero-energy resonance occurs at $\varepsilon = 6.0 \times 10^{-4}$ a.u.

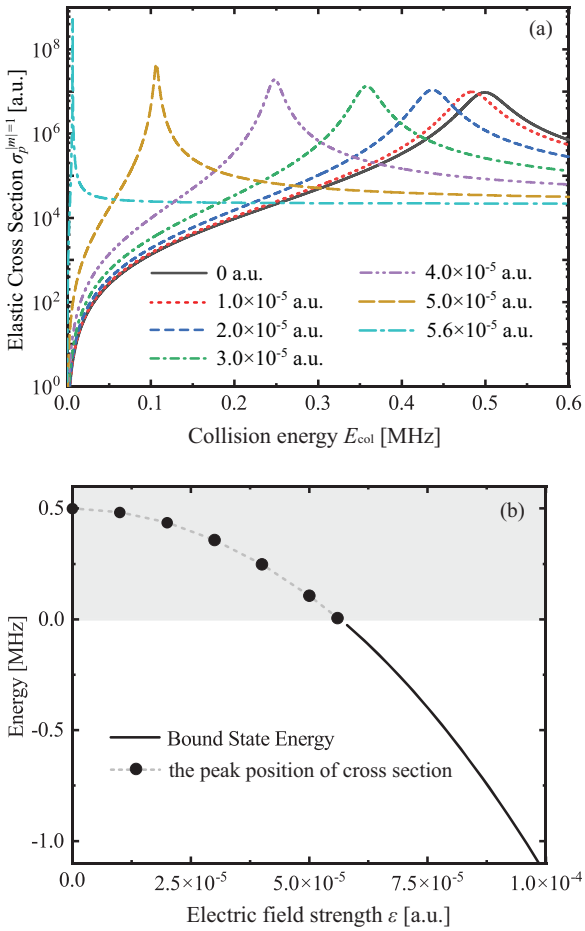

FIG. 2. (a) The p-wave cross sections $\sigma_p^{|m|=1}$ as a function of collision energy $E_{\rm col}$ at $\varepsilon = 0$ (black solid line), 1.0×10^{-5} a.u. (red dotted line), 2.0×10^{-5} a.u. (blue short-dashed line), 3.0×10^{-5} a.u. (green dot-short-dashed line), 4.0×10^{-5} a.u. (purple double-dot-short-dashed line), 5.0×10^{-5} a.u. (yellow dashed line), and 5.6×10^{-5} a.u. (light blue dot-dashed line). (b) The peak positions of p-wave cross sections $\sigma_p^{|m|=1}$ (dots) and the p-wave field-induced bound state energy (line) as a function of the electric field strength ε.

B. Wavepacket dynamics induced by a nonresonant single-cycle THz laser pulse

Now, we calculate the wavepacket dynamics of the weakly bound ^{6}Li^{23}Na molecule induced by nonresonant THz pulses, which are shown in Fig. 4. m is set to be 0. The nonresonant laser pulse couples different partial-wave states and transfers the population from the initial s-wave state to higher-partial-wave states. Different partial-wave states evolve with different spatially dependent phases. These phase factors

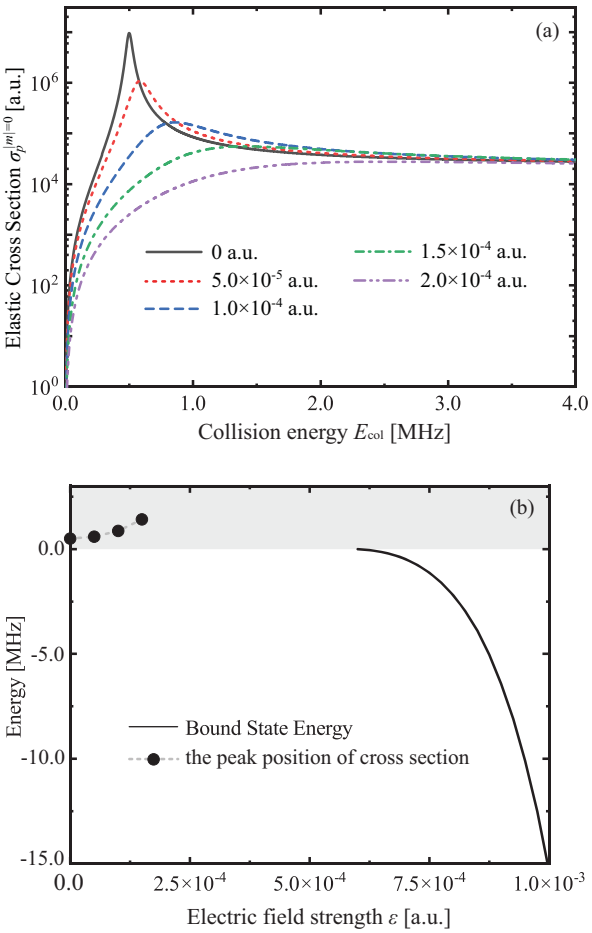

FIG. 3. (a) The p-wave cross sections $\sigma_p^{m=0}$ as a function of collision energy $E_{\rm col}$ at $\varepsilon = 0$ (black solid line), 5.0×10^{-5} a.u. (red dotted line), 1.0×10^{-4} a.u. (blue dashed line), 1.5×10^{-4} a.u. (green dot-dashed line), and 2.0×10^{-4} a.u. (purple double-dot-dashed line). (b) The peak positions of p-wave cross sections $\sigma_p^{m=0}$ (dots) and the p-wave field-induced bound state energy (line) as a function of the electric field strength ε.

imprint a time-dependent and R-dependent oscillatory pattern on $C_2(R,t)$ [22,23] and $C_1(R,t)$.

To interpret the oscillating pattern in $C_2(R,t)$ and $C_1(R,t)$, we derive the approximate expressions for $C_2(R,t)$ and $C_1(R,t)$. The wave function of the system $\Psi(R,\theta,t)$ can be divided into two parts

$$\Psi(R,\theta,t) = \Psi^{\rm even}(R,\theta,t) + \Psi^{\rm odd}(R,\theta,t), \tag{7}$$

where

$$\Psi^{\rm even}(R,\theta,t) = \sum_{l=0}^{+\infty} \Psi_{2l}(R,\theta,t) = \frac{1}{R}\sum_{l=0}^{+\infty} u_{2l}(R,t) Y_{2l,0}(\theta), \tag{8}$$

and

$$\Psi^{\rm odd}(R,\theta,t) = \sum_{l=0}^{+\infty} \Psi_{2l+1}(R,\theta,t) = \frac{1}{R}\sum_{l=0}^{+\infty} u_{2l+1}(R,t) Y_{2l+1,0}(\theta). \tag{9}$$

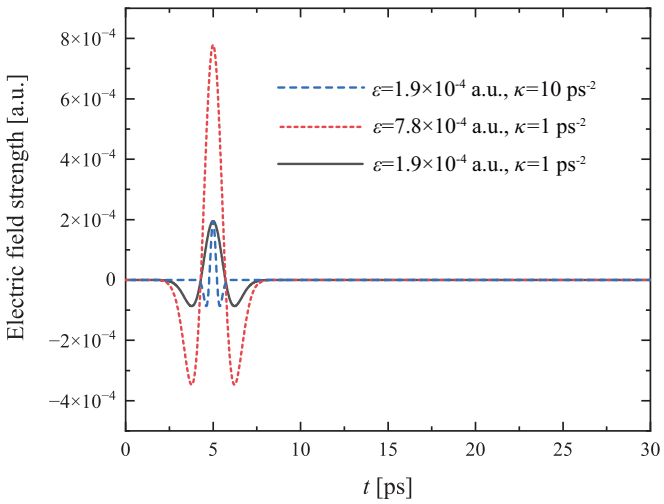

FIG. 4. The nonresonant THz laser pulses with $\varepsilon = 1.9 \times 10^{-4}$ a.u. (about 1 MV/cm), $\kappa = 1\,{\rm ps}^{-2}$, and the duration time $\delta = 2.45$ ps (the black solid line), $\varepsilon = 7.8 \times 10^{-4}$ a.u., $\kappa = 1\,{\rm ps}^{-2}$, and $\delta = 2.45$ ps (the red dotted line), $\varepsilon = 1.9 \times 10^{-4}$ a.u., $\kappa = 10\,{\rm ps}^{-2}$, and $\delta = 0.77$ ps (the blue dashed line). The center time t_0 is 5 ps.

In Eqs. (8) and (9), $u_l(R,t)$ is l-wave radial wave function and Y_{l0} is the spherical harmonic. $\Psi^{\rm even}(R,\theta,t)$ and $\Psi^{\rm odd}(R,\theta,t)$ contain the wave functions of all even and odd partial-wave channels, respectively. Inserting Eq. (7) into the numerator of Eq. (5) and considering $\int_0^\pi \Psi^{\rm even*}(R,\theta,t)\cos^2\theta\Psi^{\rm odd}(R,\theta,t)\sin\theta d\theta = 0$, $C_2(R,t)$ can be written as

$$C_2(R,t) = C_2^{\rm even}(R,t) + C_2^{\rm odd}(R,t), \tag{10}$$

where

$$C_2^{\rm even}(R,t) = \frac{\int_0^\pi \Psi^{\rm even*}(R,\theta,t)\cos^2\theta\Psi^{\rm even}(R,\theta,t)\sin\theta d\theta}{\int_0^\pi |\Psi(R,\theta,t)|^2\sin\theta d\theta}, \tag{11}$$

and

$$C_2^{\rm odd}(R,t) = \frac{\int_0^\pi \Psi^{\rm odd*}(R,\theta,t)\cos^2\theta\Psi^{\rm odd}(R,\theta,t)\sin\theta d\theta}{\int_0^\pi |\Psi(R,\theta,t)|^2\sin\theta d\theta}. \tag{12}$$

It is noted that $C_2^{\rm even}(R,t)$ defined above is identical to the $C_2(R,t)$ defined in Refs. [22,23]. When the laser intensity is low, the vast majority of the population remains in the s-wave channel. Moreover, the wave function $u_0(R,t)$ in the s-wave channel is nearly the same as the initial wave function $u_0^{\rm eigen}(R)$ [23]. If we omit the component $u_l(R,t)$ with $l > 2$ and set $u_0(R,t) \approx u_0^{\rm eigen}(R)$, we obtain

$$\Psi^{\rm even}(R,\theta,t) \approx \frac{1}{R}u_0^{\rm eigen}(R)Y_{0,0} + \frac{1}{R}u_2(R,t)Y_{2,0}, \tag{13}$$

$$\Psi^{\rm odd}(R,\theta,t) \approx \frac{1}{R}u_1(R,t)Y_{1,0}, \tag{14}$$

and

$$\Psi(R,\theta,t) \approx \frac{1}{R}u_0^{\rm eigen}(R)Y_{0,0} + \frac{1}{R}u_1(R,t)Y_{1,0} + \frac{1}{R}u_2(R,t)Y_{2,0}. \tag{15}$$

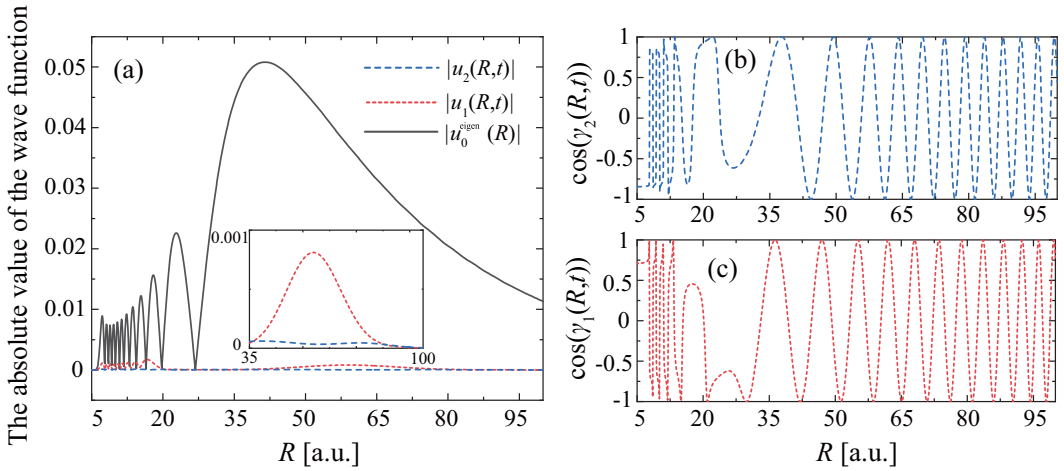

FIG. 5. (a) The absolute value of the wave function $|u_0^{\text{eigen}}(R)|$ (the black solid line), $|u_1(R,t)|$ (the red dotted line), and $|u_2(R,t)|$ (the blue dashed line) as a function of R at $t = 15$ ps. The inset shows details of $|u_1(R,t)|$ and $|u_2(R,t)|$ in the internuclear distances ranging from 35 to 100 a.u. (b) $\cos[\gamma_2(R,t)]$ and (c) $\cos[\gamma_1(R,t)]$ as a function of R at $t = 15$ ps. In the calculation, the parameters of the laser field are set to be $\varepsilon = 1.9 \times 10^{-4}$ a.u., $\kappa = 1\,\text{ps}^{-2}$, $t_0 = 5$ ps.

Inserting Eqs. (13), (14), and (15) into Eqs. (11), (12), and (6), and omitting the terms on the order of $|u_2(R,t)|^2$ and $|u_1(R,t)||u_2(R,t)|$, we obtain

$$C_2^{\text{even}}(R,t) \approx \frac{\frac{1}{3}u_0^{\text{eigen}}(R)^2 + \frac{4}{3\sqrt{5}}u_0^{\text{eigen}}(R)|u_2(R,t)|\cos[\gamma_2(R,t)]}{u_0^{\text{eigen}}(R)^2 + |u_1(R,t)|^2}, \tag{16}$$

$$C_2^{\text{odd}}(R,t) \approx \frac{\frac{3}{5}|u_1(R,t)|^2}{u_0^{\text{eigen}}(R)^2 + |u_1(R,t)|^2}, \tag{17}$$

and

$$C_1(R,t) \approx \frac{\frac{2}{\sqrt{3}}u_0^{\text{eigen}}(R)|u_1(R,t)|\cos[\gamma_1(R,t)]}{u_0^{\text{eigen}}(R)^2 + |u_1(R,t)|^2}, \tag{18}$$

where $|u_l(R,t)|$ is the absolute value of $u_l(R,t)$ and $\gamma_l(R,t)$ is the phase of $u_l(R,t)$. The initial wave function $u_0^{\text{eigen}}(R)$ is chosen to be a real function.

In the internuclear distances ranging from 35 to 100 a.u., $u_0^{\text{eigen}}(R)$ has no zero points and is much larger than $u_1(R,t)$ as shown in Fig. 5(a). Therefore, we can further neglect the $|u_1(R,t)|^2$ term in the denominator of Eqs. (16), (17), and (18), and we have

$$C_2^{\text{even}}(R,t) \approx \frac{1}{3} + \frac{4}{3\sqrt{5}}\cos[\gamma_2(R,t)]\frac{|u_2(R,t)|}{u_0^{\text{eigen}}(R)}, \tag{19}$$

$$C_2^{\text{odd}}(R,t) \approx \frac{3}{5}\frac{|u_1(R,t)|^2}{u_0^{\text{eigen}}(R)^2}, \tag{20}$$

$$C_1(R,t) \approx \frac{2}{\sqrt{3}}\cos[\gamma_1(R,t)]\frac{|u_1(R,t)|}{u_0^{\text{eigen}}(R)}. \tag{21}$$

The approximation expression of $C_2^{\text{even}}(R,t)$ Eq. (19) has been obtained in Ref. [23].

Figures 6(a) to 6(d) show numerically calculated $C_2(R,t)$, $C_2^{\text{even}}(R,t)$, $C_2^{\text{odd}}(R,t)$, and $C_1(R,t)$ in the internuclear distances ranging from 35 to 100 a.u., respectively. The parameters of the laser field are $\varepsilon = 1.9 \times 10^{-4}$ a.u. (about 1 MV/cm), $\kappa = 1$ ps^{-2}, $t_0 = 5$ ps and the laser field is shown by the black solid line in Fig. 4. For comparison, Figs. 6(e) to 6(h) show the results calculated according to Eqs. (10), (19), (20), and (21). The $u_0^{\text{eigen}}(R)$, $u_1(R,t)$, and $u_2(R,t)$ needed in Eqs. (19), (20), and (21) are obtained from the fully numerical calculation. Comparing the upper and lower panels of Fig. 6, it can be seen that the approximate expressions reproduce the numerical results. From Figs. 6(b) and 6(f) we observe an outgoing oscillatory pattern in $C_2^{\text{even}}(R,t)$. Similar oscillatory patterns of $C_2(R,t)$ were observed in the studies with $^4He_2$ molecules, and were found due to the interference between the remaining portion of the initial s-wave state and the d-wave dissociating wavepacket induced by the laser pulse [22,23]. In this range of internuclear distance, $u_0^{\text{eigen}}(R)$ and $|u_2(R,t)|$ do not oscillate as shown in Fig. 5(a). Thus, according to Eq. (19), we attribute the oscillatory pattern to the oscillations in $\cos[\gamma_2(R,t)]$, as shown in Fig. 5(b). For homonuclear molecules, one can extract the phase $\gamma_2(R,t)$ of the wave function $u_2(R,t)$ in the d-wave channel by measuring $C_2^{\text{even}}(R,t)$ [23]. From Figs. 6(c) and 6(g) we observe an outgoing pattern in $C_2^{\text{odd}}(R,t)$. However, there is no oscillation in this outgoing pattern. This is because, of all the odd-partial-wave channels, the vast majority of the population is present in the p-wave channel. Therefore, there is no notable interference between the wave function in p-wave channel and the wave functions in other higher odd-partial-wave channels. $C_2^{\text{odd}}(R,t)$ in Figs. 6(c) and 6(g) is small. This is due to the fact that $C_2^{\text{odd}}(R,t)$ is proportional to the ratio of $|u_1(R,t)|$ and $u_0^{\text{eigen}}(R)$ according to Eq. (20), and $|u_1(R,t)|$ is smaller compared with $u_0^{\text{eigen}}(R)$ as shown in Fig. 5(a). Since $C_2^{\text{even}}(R,t)$ is much larger than $C_2^{\text{odd}}(R,t)$, $C_2(R,t)$ is mainly determined by $C_2^{\text{even}}(R,t)$, as shown in Figs. 6(a) and 6(e). For heteronuclear molecules, one can extract the phase $\gamma_2(R,t)$ of the wave function $u_2(R,t)$ in the d-wave channel by measuring $C_2(R,t)$. Similar to $C_2^{\text{even}}(R,t)$, we observe the outgoing oscillatory pattern in $C_1(R,t)$, as shown in Figs. 6(d) and 6(h). According to Eq. (21), we attribute the oscillatory pattern in $C_1(R,t)$ to the interference between the remaining

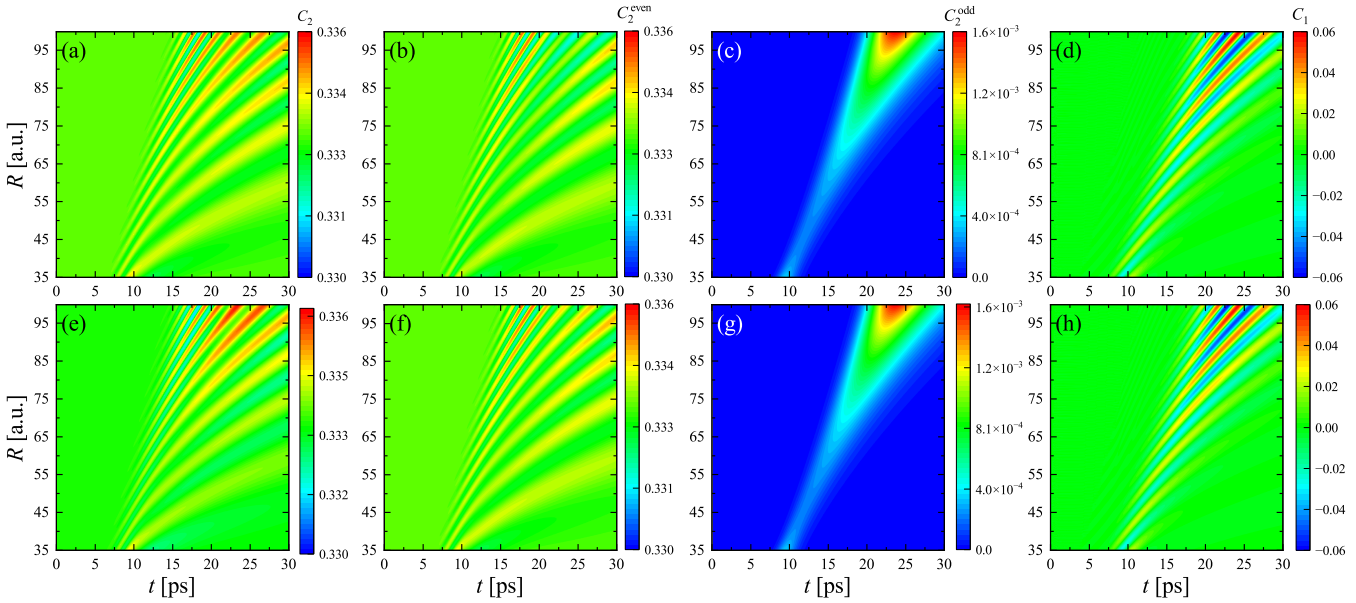

FIG. 6. (a), (e) $C_2(R,t)$, (b), (f) $C_2^{\rm even}(R,t)$, (c), (g) $C_2^{\rm odd}(R,t)$, (d), (h) $C_1(R,t)$ as functions of R and t in the internuclear distances ranging from 35 to 100 a.u. (a)–(d) are from full quantum calculation, (e)–(h) are calculated with Eqs. (10), (19), (20), and (21). In the calculation, the parameters of the laser field are set to be $\varepsilon = 1.9 \times 10^{-4}$ a.u., $\kappa = 1\,\mathrm{ps}^{-2}$, $t_0 = 5$ ps.

portion of the initial s-wave state and the p-wave dissociating wavepacket. In the range of internuclear distance considered in Fig. 6, $u_0^{\rm eigen}(R)$ and $|u_1(R,t)|$ do not oscillate as shown in Fig. 5(a). The oscillatory pattern of $C_1(R,t)$ is due to the oscillations in $\cos[\gamma_1(R,t)]$, as shown in Fig. 5(c). As a result, one can extract the phase $\gamma_1(R,t)$ of the wave function $u_1(R,t)$ in p-wave channel by measuring $C_1(R,t)$.

Figures 7(a) to 7(d) show numerically calculated $C_2(R,t)$, $C_2^{\rm even}(R,t)$, $C_2^{\rm odd}(R,t)$, and $C_1(R,t)$ in the internuclear distances ranging from 5 to 35 a.u., respectively. As shown in Fig. 5(a), $u_0^{\rm eigen}(R)$ has nodes in the range of R from 5 to 35 a.u. The approximate expressions (19), (20), and (21) fail in this region, while Eqs. (16), (17), and (18) are still valid. The results calculated with Eqs. (10), (16), (17), and (18) are presented in Figs. 7(e) to 7(h), respectively. Comparing the upper and lower panels of Fig. 7, it can be seen that the approximate expressions reproduce the fully numerical results. When R is far away from the nodes of $u_0^{\rm eigen}(R)$, $u_1(R,t)$, and $u_2(R,t)$ are small quantities compared with $u_0^{\rm eigen}(R)$ as shown in Fig. 5(a), and is approximated

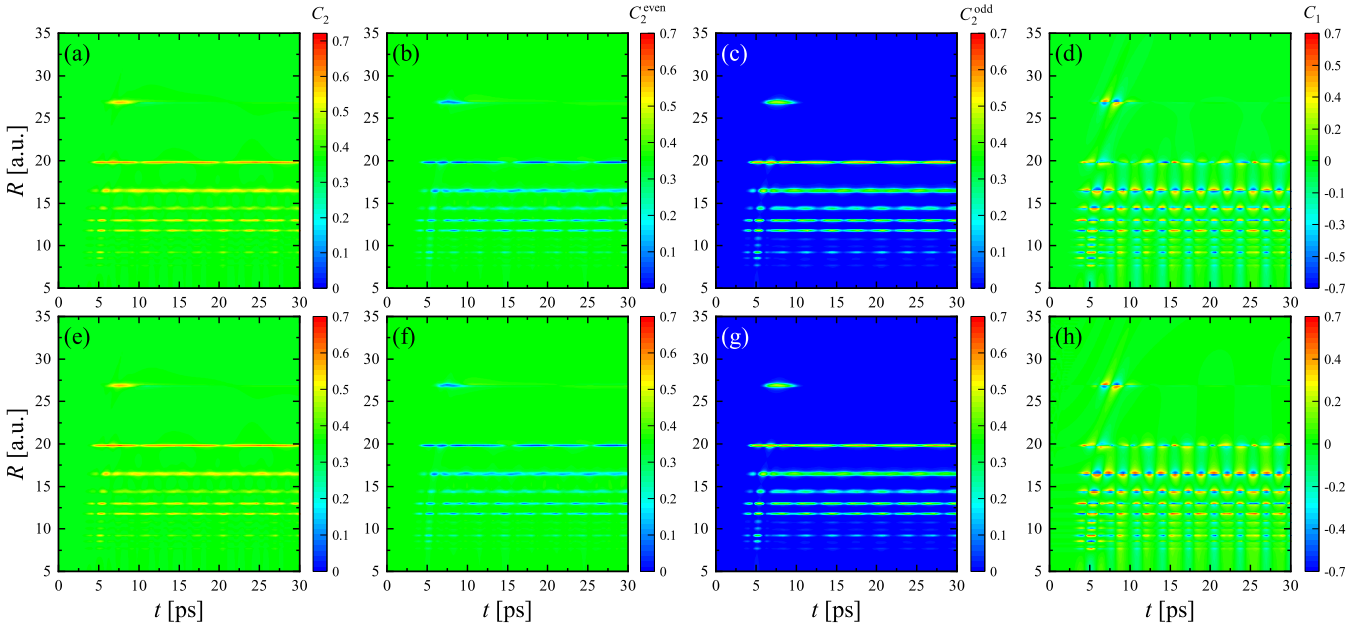

FIG. 7. (a), (e) $C_2(R,t)$, (b), (f) $C_2^{\rm even}(R,t)$, (c), (g) $C_2^{\rm odd}(R,t)$, (d), (h) $C_2(R,t)$ as functions of R and t in the internuclear distances ranging from 5 to 35 a.u. (a)–(d) are from full quantum calculation, (e)–(h) are calculated with Eqs. (10) (16), (17), and (18). In the calculation, the parameters of the laser field are set to be $\varepsilon = 1.9 \times 10^{-4}$ a.u., $\kappa = 1\,\mathrm{ps}^{-2}$, $t_0 = 5$ ps.

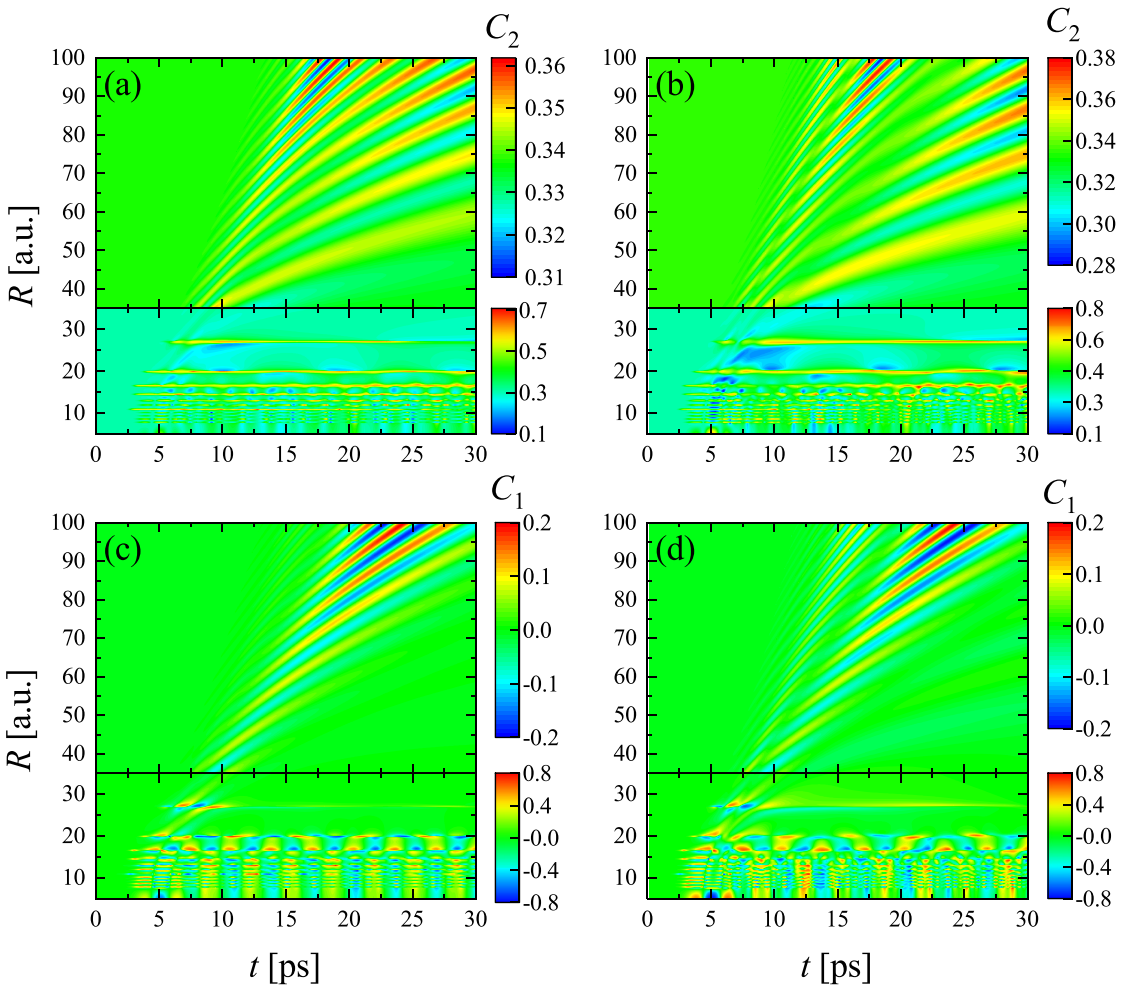

FIG. 8. (a) $C_2(R,t)$ and (c) $C_1(R,t)$ as a function of R and t calculated with $\varepsilon = 7.8 \times 10^{-4}$ a.u., (b) $C_2(R,t)$, and (d) $C_1(R,t)$ calculated with $\varepsilon = 1.6 \times 10^{-3}$ a.u.. κ is 1 ps^{-2}, the duration time δ is 2.45 ps, and the central time t_0 is 5 ps.

to be 0. According to Eqs. (16) and (17), $C_2^{\text{even}}(R,t)$ and $C_2^{\text{odd}}(R,t)$ approximately equal 1/3 and 0, respectively. $C_2(R,t)$ approximately equals 1/3, which is the sum of $C_2^{\text{even}}(R,t)$ and $C_2^{\text{odd}}(R,t)$. According to Eq. (18), $C_1(R,t)$ approximately equals 0. At the nodes of $u_0^{\text{eigen}}(R)$, $u_0^{\text{eigen}}(R)$ is 0. According to Eqs. (16) and (17), $C_2^{\text{even}}(R,t)$ is zero, and $C_2^{\text{odd}}(R,t)$ is 3/5. $C_2(R,t)$ approaches the extreme value of 3/5. According to Eq. (18), $C_1(R,t)$ is zero. When R is slightly away from the nodes of $u_0^{\text{eigen}}(R)$, $u_0^{\text{eigen}}(R)$, and $u_1(R,t)$ have the same order of magnitude. Then $C_1(R,t)$ deviates from 0, and takes extreme value when $\frac{\partial C_1(R,t)}{\partial R} = 0$. The above analyses have been confirmed in Fig. 7, and suggest that we can map out the nodes of the initial wavefunction by experimentally measuring $C_2(R,t)$ or $C_1(R,t)$. In the previous studies with $^4He_2$ molecule [22], $C_2(R,t)$ does not possess similar structures since the potential curve of $^4He_2$ molecule supports only one bound state and the wave function of the initial bound state has no nodes.

As shown in Figs. 7(c) and 7(g) and 7(d) and 7(h), $C_2^{\text{odd}}(R,t)$ and $C_1(R,t)$ oscillate over time t when R is fixed near the nodes of $u_0^{\text{eigen}}(R)$, and the period of this oscillation is about 3.2 ps. This oscillation is due to the superposition of the $v = 7$ and $v = 8$ vibrational states in the p-wave channel, which are the most populated states in the p-wave channel after the laser pulse is applied. Energies of these two states are 9.58×10^{-5} a.u. and 4.69×10^{-5} a.u., respectively. The timescale determined by the energy difference between these two p-wave states is 3.1 ps, which is close to the period of the oscillations 3.2 ps. $C_2^{\text{even}}(R,t)$ also oscillates over time t as shown in Figs. 7(b) and 7(f). However, this oscillation is multifrequency. This is because multiple vibrational states in the d-wave channel are populated, and the population of these states are comparable. $C_2(R,t)$ is the sum of $C_2^{\text{even}}(R,t)$ and $C_2^{\text{odd}}(R,t)$, So the oscillation over time t in $C_2(R,t)$ is also multifrequency, as shown in Figs. 7(a) and 7(e).

The parameters of the laser pulse will affect the dynamics. We first discuss the influence of electric-field amplitude ε on $C_2(R,t)$ and $C_1(R,t)$. Figures 8(a) and 8(c) show $C_2(R,t)$ and $C_1(R,t)$ as a function of R and t with $\varepsilon = 7.8 \times 10^{-4}$ a.u., Figs. 8(b) and 8(d) show $C_2(R,t)$ and $C_1(R,t)$ with $\varepsilon = 1.6 \times 10^{-3}$ a.u.κ is 1 ps^{-2} and the duration time δ is 2.45 ps. As ε increases, more population is transferred from the initial s-wave channel to high-partial-wave channels, and the maxima of $C_2(R,t)$ and $C_1(R,t)$ deviate more from their initial values 1/3 and 0, respectively. As shown in Fig. 4, there are secondary peaks in the laser pulse besides the main peak.

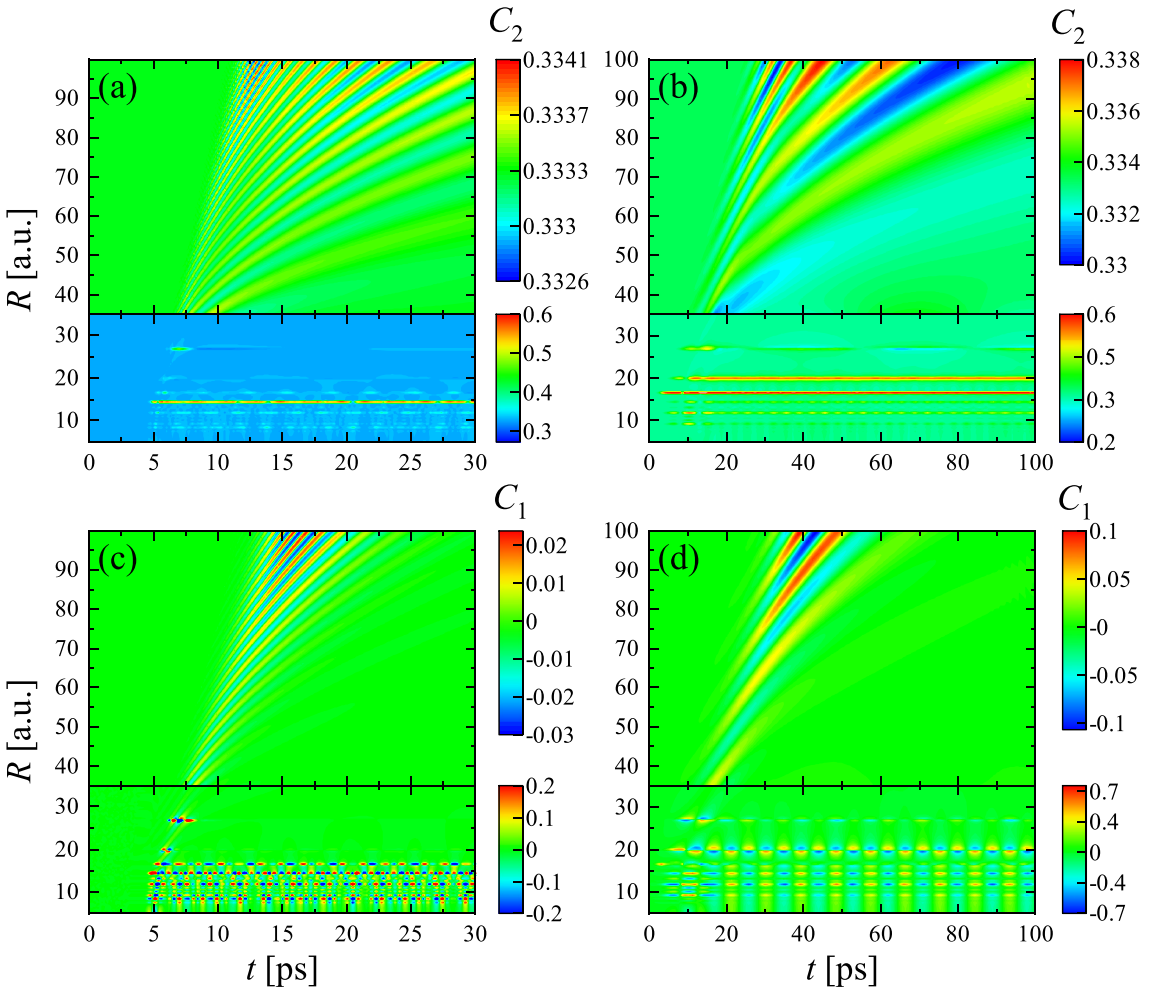

FIG. 9. (a) $C_2(R,t)$ and (c) $C_1(R,t)$ calculated with $\kappa = 10\ \mathrm{ps}^{-2}$, $\delta = 0.77$ ps, and $t_0 = 5$ ps. (b) $C_2(R,t)$ and (d) $C_1(R,t)$ calculated with $\kappa = 0.1\ \mathrm{ps}^{-2}$, $\delta = 7.8$ ps, and $t_0 = 10$ ps. The electric field amplitude of the laser pulse is $\varepsilon = 1.9 \times 10^{-4}$ a.u.

When ε is 7.8×10^{-4} a.u., only the main peak can induce dissociating wavepacket, as shown in Figs. 8(a) and 8(c). When ε is 1.6×10^{-3} a.u., the secondary peaks are strong enough to induce dissociating wavepacket, as shown in Figs. 8(b) and 8(d).

The duration of the laser pulse also affects the dynamics. Figures 9(a) and 9(c) show $C_2(R,t)$ and $C_1(R,t)$ calculated with $\kappa = 10\,\mathrm{ps}^{-2}$, $\delta = 0.77$ ps, and $t_0 = 5$ ps. Figures 9(b) and 9(d) show $C_2(R,t)$ and $C_1(R,t)$ calculated with $\kappa = 0.1\,\mathrm{ps}^{-2}$, $\delta = 7.8$ ps, and $t_0 = 10$ ps. The electric-field amplitude of the laser pulse is $\varepsilon = 1.9 \times 10^{-4}$ a.u. As δ increases, the energy of laser pulse increases. More population is transferred from the initial s-wave channel to high-partial-wave channels, and the maxima of $C_2(R,t)$ and $C_1(R,t)$ deviate more from their initial values $1/3$ and 0, respectively. Meanwhile, as δ increases, the variation of the laser field is less intense, as shown in Fig. 4. There will be less bound and scattering states populated in the high-partial-wave channels. This is reflected by the following two facts. In the internuclear distances ranging from 5 to 35 a.u., the oscillations of $C_2(R,t)$ and $C_1(R,t)$ over time in Figs. 9(b) and 9(d) are simpler than those in Figs. 9(a) and 9(c). In the internuclear distances ranging from 35 to 100 a.u., the interference fringes are broad in Figs. 9(b) and 9(d).

C. Effect of the quasibound state on the wavepacket dynamics

In this section, we investigate the influence of a quasibound state on the wavepacket dynamics of a weakly bound molecule. ε is set to be 2.0×10^{-3} a.u., and the peak electric

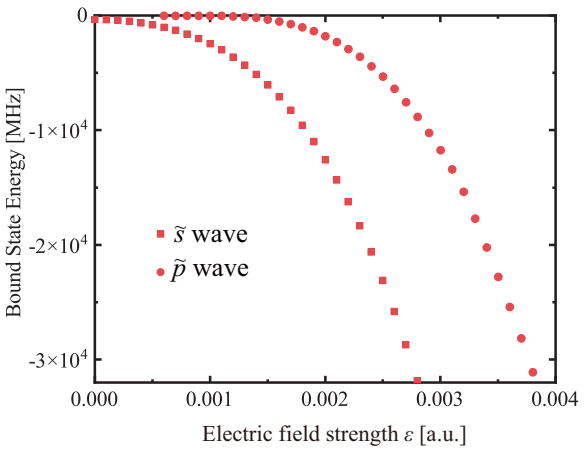

FIG. 10. The energy of the $\tilde{s}$-wave bound state (squares) and the $\tilde{p}$-wave electric-field-induced bound state (dots) as a function of the electric field strength ε.

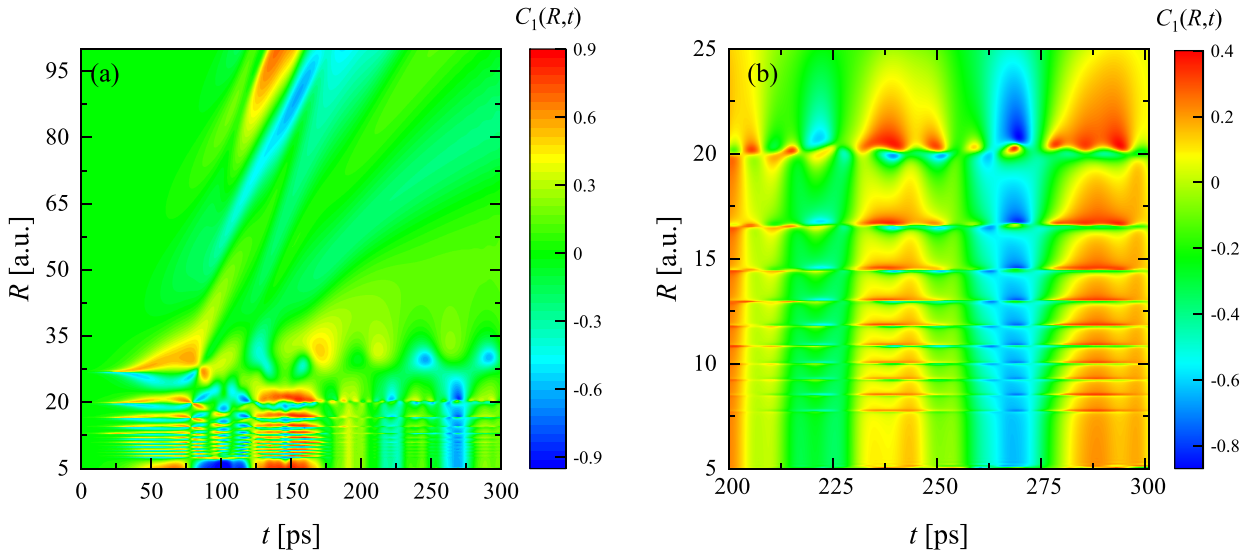

FIG. 11. (a) $C_1(R,t)$ as a function of the internuclear distance R and time t. (b) The details of $C_1(R,t)$ in the small internuclear distance after the laser pulse finished, i.e., $t > 200$ ps. In the calculation, $\varepsilon = 2.0 \times 10^{-3}$ a.u., $\kappa = 10^{-3}$ ps^{-2}, and the according duration time $\delta = 77$ ps.

field is strong enough to tune the p-wave quasibound state into an bound state, as indicated in Fig. 10. κ is chosen to be 10^{-3} ps^{-2} and the corresponding duration time δ is 77 ps. The laser field varies slowly as a function of time and the populations in the high-partial-wave channels are concentrated in a few bound and scattering states. We choose $C_1(R,t)$ to visualize the dynamic process, which is shown in Fig. 11. In the internuclear distances ranging from 5 to 35 a.u., the oscillations of $C_1(R,t)$ as a function of t are observed when the THz pulse is applied, i.e., from 0 to 200 ps, as shown in Fig. 11(a). In Ref. [22], similar oscillations of $C_2(R,t)$ were observed. During the plateau of the stretched Gaussian pulse adopted in Ref. [22], the period of the oscillation is precisely inversely proportional to the energy difference between the intrinsic bound state and the field-induced bound state. In our case, the electric field of the laser field is time dependent during the whole period of the THz pulse, as shown in Fig. 4. The energies of the intrinsic $\tilde{s}$-wave bound state and the field-induced $\tilde{p}$-wave bound state varies with electric field, as shown in Fig. 10. As a result, the period of the oscillation observed in Fig. 11 cannot be simply determined as in Ref. [22].

For clarity, the $C_1(R,t)$ in short-range region is shown in Fig. 11(b). It is seen that $C_1(R,t)$ oscillates as a function of time after the laser pulse finished at $t = 200$ ps. To interpret these oscillations, the probability densities of s- and p-wave states are shown in Fig. 12. As shown in Fig. 12, the s-wave probability density is dominant after the laser pulse finished. This is due to the fact that the initial state is an s-wave bound state. Nevertheless, the p-wave probability densities do not vanish in the short-range region at the end of the laser pulse, as shown in Figs. 12(b). Moreover the s-wave and p-wave probability densities in the short-range region show clear oscillations after $t = 200$ ps. This results in the oscillations of $C_1(R,t)$.

We further calculate populations of the vibrational levels and scattering levels at the end of laser pulse, which are shown in Fig. 13. For the s-wave channel, the last bound level with vibrational quantum number $v = 11$ (the initial state) and the last but second bound level with $v = 10$ are populated, as

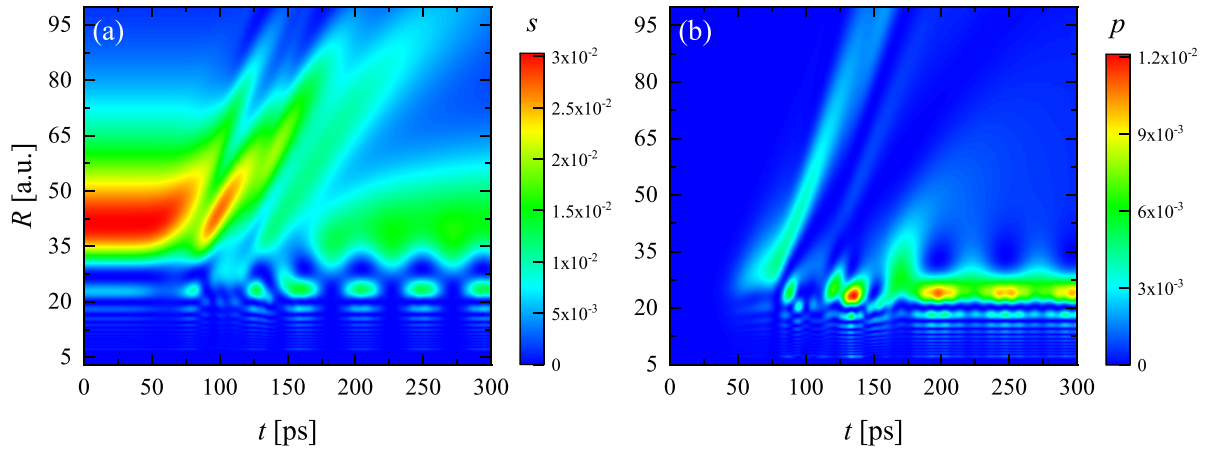

FIG. 12. The (a) s- and (b) p-wave probability densities as a function of the internuclear distance R and time t.

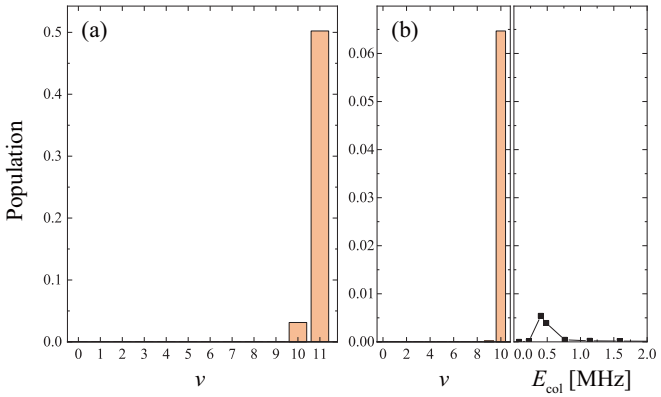

FIG. 13. The population as functions of the vibrational quantum number v for the bound states and the collision energy E_{col} for the scattering states at the end of laser pulse in (a) s- and (b) p-wave channels.

shown in Fig. 13(a). The oscillations of the s-wave probability density in the short-range region after $t = 200$ ps is attributed to the superposition of these two vibrational levels. The period of the oscillations in Fig. 12(a) is 45.2 ps, which is close to the timescale of 45.3 ps determined by the energy difference between the two s-wave vibrational levels. Among all the p-wave bound levels, only the last bound level with $v = 10$ is notably populated as shown in Fig. 13(b). For the population of the scattering state there is a peak at collision energy $E_{col} = 0.5$ MHz, which is exactly the position of the quasibound state in the absence of laser field. It is noted that the box-normalized wave function [52] is adopted to describe the scattering state. The oscillations of the p-wave probability density after $t = 200$ ps observed in Fig. 12(b) is attributed to the superposition of the last vibrational level with $v = 10$ and the quasibound state at $E_{col} = 0.5$ MHz. The period of the oscillation in Fig. 12(b) is 50.2 ps, which is roughly close to the timescale of 49.0 ps determined by the energy difference between the last p-wave bound state and the quasibound state. For the $^4He_2$ molecule studied in Ref. [22], there is only one s-wave bound state in the absence of laser field. As a result, there is no superposition between bound states and there is no superposition between the bound state and quasibound state of the same partial-wave channel at the end of the laser pulse.

IV. CONCLUSION

In this work, a $^6Li^{23}Na$ molecule in a $a^3\Sigma^+$ state is chosen as a prototype to investigate the control of a weakly bound heteronuclear molecule by an external static electric field as well as a nonresonant single-cycle THz pulse. We find that the energy of the high-partial-wave quasibound states with $m = 0$ increases initially with the increase of the electric field strength and finally becomes a field-induced bound state when the electric field is strong enough. The energies of the states with $|m| \neq 0$ decrease monotonically with the increase of the electric field. Both the $m = 0$ and $|m| \neq 0$ quasibound state can cross the threshold and produce a zero-energy electric-field-induced resonance. These calculations complete the theory about the properties of bound and scattering states of a heteronuclear alkali-metal two-body collision complex in a static electric field [20].

After that, we investigate the dynamics of a $^6Li^{23}Na$ molecule in the weakest s-wave bound state induced by a nonresonant THz laser pulse. We show that the orientation signals, in additon to the alignment signals, can be measured to study the dynamics of weakly bound heteronuclear molecules. The interferences between the initial s-wave bound state and the p-wave dissociating wavepacket can be indicated by the orientation signals, and one can extract the phase of the wavepacket in the p-wave channel from the orientation signals. After the laser pulse is finished, interferences between bound states and between the bound state and quasibound state are observed for the $^6Li^{23}Na$ molecule, which is absent in the study with the $^4He_2$ molecule [22]. The effects of the electric-field amplitude and the duration time of the laser pulse on the wavepacket dynamics are investigated. Furthermore, we show that one can map out the nodes of the probability density of weakly bound $^6Li^{23}Na$ molecules by measuring the wavepacket dynamics. Our results provide compelling evidence for the feasible tunability of the weakly bound heteronuclear alkali-metal diatomic molecules by a well-designed nonresonant laser pulse.

Currently, the electric-field amplitude of the THz laser pulse can reach several MV/cm (10^{-3} a.u.) in a broad spectrum range [53,54], which is on the same order of the electric-field amplitude used in this work. In Ref. [15], an experimental apparatus combining an optical dipole trap with a reaction microscope was presented. Adding the THz laser pulse in such an apparatus will allow one to observe experimentally the dynamics discussed in this work.

ACKNOWLEDGMENTS

This work was supported by the National Natural Science Foundation of China (Grants No. 12104082 and No. 12241409), the National Key R&D Program of China (Grant No. 2018YFA0306503), and the Innovation Program for Quantum Science and Technology (Grant No. 2021ZD0302100).

[1] T. Köhler, K. Góral, and P. S. Julienne, Rev. Mod. Phys. **78**, 1311 (2006).
[2] T. Langen, G. Valtolina, D. Wang, and J. Ye, arXiv:2305.13445.
[3] T. Franzen, B. Pollklesener, C. Sillus, and A. Görlitz, Phys. Rev. A **107**, 023114 (2023).
[4] X. He, K. Wang, J. Zhuang, P. Xu, X. Gao, R. Guo, C. Sheng, M. Liu, J. Wang, J. Li, G. V. Shlyapnikov, and M. Zhan, Science **370**, 331 (2020).
[5] C. Maury, B. Bakkali-Hassani, G. Chauveau, F. Rabec, S. Nascimbène, J. Dalibard, and J. Beugnon, Phys. Rev. Res. **5**, L012020 (2023).
[6] M. Duda, X.-Y. Chen, R. Bause, A. Schindewolf, I. Bloch, and X.-Y. Luo, Phys. Rev. A **107**, 053322 (2023).
[7] A. Z. Lam, N. Bigagli, C. Warner, W. Yuan, S. Zhang, E. Tiemann, I. Stevenson, and S. Will, Phys. Rev. Res. **4**, L022019 (2022).

[8] G. Quéméner, J. L. Bohn, and J. F. E. Croft, Phys. Rev. Lett. **131**, 043402 (2023).

[9] H. Yang, J. Cao, Z. Su, J. Rui, B. Zhao, and J.-W. Pan, Science **378**, 1009 (2022).

[10] X.-Y. Chen, S. Biswas, S. Eppelt, A. Schindewolf, F. Deng, T. Shi, S. Yi, T. A. Hilker, I. Bloch, and X.-Y. Luo, Nature (London) **626**, 283 (2024).

[11] J. S. Rosenberg, L. Christakis, E. Guardado-Sanchez, Z. Z. Yan, and W. S. Bakr, Nat. Phys. **18**, 1062 (2022).

[12] Y. Kiefer, M. Hachmann, and A. Hemmerich, Nat. Phys. **19**, 794 (2023).

[13] J. Rui, H. Yang, L. Liu, D.-C. Zhang, Y.-X. Liu, J. Nan, Y.-A. Chen, B. Zhao, and J.-W. Pan, Nat. Phys. **13**, 699 (2017).

[14] B. Zhao and J.-W. Pan, Chem. Soc. Rev. **51**, 1685 (2022).

[15] N. Kurz, D. Fischer, T. Pfeifer, and A. Dorn, Rev. Sci. Instrum. **92**, 123202 (2021).

[16] M. Borkowski, Phys. Rev. Lett. **120**, 083202 (2018).

[17] K. H. Leung, B. Iritani, E. Tiberi, I. Majewska, M. Borkowski, R. Moszynski, and T. Zelevinsky, Phys. Rev. X **13**, 011047 (2023).

[18] M. Borkowski, A. A. Buchachenko, R. Ciury Lo, P. S. Julienne, H. Yamada, Y. Kikuchi, Y. Takasu, and Y. Takahashi, Sci. Rep. **9**, 14807 (2019).

[19] R. González-Férez and P. Schmelcher, New J. Phys. **11**, 055013 (2009).

[20] Z.-A. Li, Z.-W. Wang, G.-R. Wang, and S.-L. Cong, Phys. Rev. A **101**, 053409 (2020).

[21] M. Tomza, R. González-Férez, C. P. Koch, and R. Moszynski, Phys. Rev. Lett. **112**, 113201 (2014).

[22] Q. Guan and D. Blume, Phys. Rev. A **99**, 033416 (2019).

[23] M. Kunitski, Q. Guan, H. Maschkiwitz, J. Hahnenbruch, S. Eckart, S. Zeller, A. Kalinin, M. Schöffler, L. P. H. Schmidt, T. Jahnke, D. Blume, and R. Dörner, Nat. Phys. **17**, 174 (2021).

[24] C. Ospelkaus, S. Ospelkaus, L. Humbert, P. Ernst, K. Sengstock, and K. Bongs, Phys. Rev. Lett. **97**, 120402 (2006).

[25] C. Weber, G. Barontini, J. Catani, G. Thalhammer, M. Inguscio, and F. Minardi, Phys. Rev. A **78**, 061601(R) (2008).

[26] M. P. Köppinger, D. J. McCarron, D. L. Jenkin, P. K. Molony, H.-W. Cho, S. L. Cornish, C. R. Le Sueur, C. L. Blackley, and J. M. Hutson, Phys. Rev. A **89**, 033604 (2014).

[27] C.-H. Wu, J. W. Park, P. Ahmadi, S. Will, and M. W. Zwierlein, Phys. Rev. Lett. **109**, 085301 (2012).

[28] A.-C. Voigt, M. Taglieber, L. Costa, T. Aoki, W. Wieser, T. W. Hänsch, and K. Dieckmann, Phys. Rev. Lett. **102**, 020405 (2009).

[29] F. Wang, X. He, X. Li, B. Zhu, J. Chen, and D. Wang, New J. Phys. **17**, 035003 (2015).

[30] M.-S. Heo, T. T. Wang, C. A. Christensen, T. M. Rvachov, D. A. Cotta, J.-H. Choi, Y.-R. Lee, and W. Ketterle, Phys. Rev. A **86**, 021602(R) (2012).

[31] T. Takekoshi, L. Reichsöllner, A. Schindewolf, J. M. Hutson, C. R. Le Sueur, O. Dulieu, F. Ferlaino, R. Grimm, and H.-C. Nägerl, Phys. Rev. Lett. **113**, 205301 (2014).

[32] C. Chin, R. Grimm, P. Julienne, and E. Tiesinga, Rev. Mod. Phys. **82**, 1225 (2010).

[33] S. Grishkevich, P.-I. Schneider, Y. V. Vanne, and A. Saenz, Phys. Rev. A **81**, 022719 (2010).

[34] T. M. Rvachov, H. Son, A. T. Sommer, S. Ebadi, J. J. Park, M. W. Zwierlein, W. Ketterle, and A. O. Jamison, Phys. Rev. Lett. **119**, 143001 (2017).

[35] R. V. Krems, Phys. Rev. Lett. **96**, 123202 (2006).

[36] D. Chakraborty, J. Hazra, and B. Deb, J. Phys. B **44**, 095201 (2011).

[37] B. Friedrich and D. Herschbach, Phys. Rev. Lett. **74**, 4623 (1995).

[38] M. Muramatsu, M. Hita, S. Minemoto, and H. Sakai, Phys. Rev. A **79**, 011403(R) (2009).

[39] L. Xu, I. Tutunnikov, E. Gershnabel, Y. Prior, and I. S. Averbukh, Phys. Rev. Lett. **125**, 013201 (2020).

[40] L. H. Coudert, J. Chem. Phys. **146**, 024303 (2017).

[41] M. Marinescu and L. You, Phys. Rev. Lett. **81**, 4596 (1998).

[42] B. Deb and L. You, Phys. Rev. A **64**, 022717 (2001).

[43] Z. Li and R. V. Krems, Phys. Rev. A **75**, 032709 (2007).

[44] M. Iñarrea, J. P. Salas, González-Férez, and P. Schmelcher, Phys. Lett. A **374**, 457 (2010).

[45] T. M. Rvachov, H. Son, J. J. Park, S. Ebadi, M. W. Zwierlein, W. Ketterlea, and A. O. Jamisona, Phys. Chem. Chem. Phys. **20**, 4739 (2018).

[46] M. Aymar and O. Dulieu, J. Chem. Phys. **122**, 204302 (2005).

[47] V. Kokoouline, O. Dulieu, R. Kosloff, and F. Masnou-Seeuws, J. Chem. Phys. **110**, 9865 (1999).

[48] K. Willner, O. Dulieu, and F. Masnou-Seeuws, J. Chem. Phys. **120**, 548 (2004).

[49] D. E. Manolopoulos, J. Chem. Phys. **85**, 6425 (1986).

[50] H. Tal-Ezer and R. Kosloff, J. Chem. Phys. **81**, 3967 (1984).

[51] R. Kosloff, J. Phys. Chem. **92**, 2087 (1988).

[52] C. P. Koch, R. Kosloff, E. Luc-Koenig, F. Masnou-Seeuws, and A. Crubellier, J. Phys. B **39**, S1017 (2006).

[53] X. Wu, D. Kong, S. Hao, Y. Zeng, X. Yu, B. Zhang, M. Dai, S. Liu, J. Wang, Z. Ren, S. Chen, J. Sang, K. Wang, D. Zhang, Z. Liu, J. Gui, X. Yang, Y. Xu, Y. Leng, Y. Li *et al.*, Adv. Mater. **35**, 2208947 (2023).

[54] R. Rouzegar, A. L. Chekhov, Y. Behovits, B. R. Serrano, M. A. Syskaki, C. H. Lambert, D. Engel, U. Martens, M. Münzenberg, M. Wolf, G. Jakob, M. Kläui, T. S. Seifert, and T. Kampfrath, Phys. Rev. Appl. **19**, 034018 (2023).